Optics & Laser Technology 164 (2023) 109431

Contents lists available at ScienceDirect

Optics and Laser Technology

journal homepage: www.elsevier.com/locate/optlastec

Full length article

Laser direct writing graphene assembly film for realizing plasmon-induced transparency at terahertz region

Bohan Zhang [a,c], Xiaotian Huang [b,c], Ge Chen [b,c], Zhe Wang [d], Wei Qian [d], Zixin Zhang [d], Weiqi Cai [e], Kang Du [a,c], Cai Zhou [a,c], Tingting Wang [a,c], Wei Zhu [a,c,*], Daping He [d], Shengxiang Wang [a,c,*]

[a] School of Mathematical and Physical Sciences, Wuhan Textile University, Wuhan 430200, PR China
[b] School of Electronic and Electrical Engineering, Wuhan Textile University, Wuhan 430200, PR China
[c] State Key Laboratory of New Textile Materials and Advanced Processing Technologies, Wuhan Textile University, Wuhan 430200, PR China
[d] Hubei Engineering Research Center of RF-Microwave Technology and Application, Wuhan University of Technology, Wuhan 430070, PR China
[e] Research Institute for Special Structures of Aeronautical Composite AVIC, The Aeronautical Special Key Lab for High Performance Electromagnetic Windows, Jinan 280023, PR China

ARTICLE INFO

Keywords:
Laser direct writing
Graphene assembly film
Metasurfaces
Large area
Plasmon-induced transparency

ABSTRACT

Terahertz (THz) metasurfaces, which combine the low energy and high transmission properties of THz wave with the flexible modulation characteristic of electromagnetic derived from metasurfaces, have made tremendous research progress in the field of filtering, security, 6G communications and bio-sensing. However, the practical application of THz metasurfaces is limited by the complex preparation process and the small sample area. Herein, we propose a large-scale flexible metasurface by introducing laser direct writing (LDW) fabrication method which can directly ablate the designed patterns on the wafer through the heat of laser. This proposed flexible metasurface can achieve a typical plasmon-induced transparency (PIT) effect in the reflection spectra at terahertz region by introducing a novel graphene assembly film (GAF) whose conductivity reaches 1.1×10^6 S·m^{-1} that is close to metals. In addition, the LDW processing method ablates the designed pattern on the GAF by laser heat, which only takes 30 min to complete the large area of 229 mm × 305 mm metasurface owing to fast-scanning speed of the mirrors and large scanning area of the LDW system, and the ablation precision can reach 50 μm. It is foreseen that this processing method using LDW on GAF, with its advantages of rapid fabrication, large area, low cost and flexibility, will provide a new way for the development of THz devices.

1. Introduction

THz waves [1], the wavelength located between the microwave and the infrared bands, have great application potentials in the fields of 6G communication [2], material detection [3], defense and security [4], and bio-sensing [5–7] due to the excellent characteristics of it such as low energy, high transmission, strong coherence and molecular fingerprint [8,9]. However, the deprivation of the devices for generating and manipulating THz waves has severely restricted the development of THz science and technology. In addition, the relatively weak interaction between the THz wave and matters has brought additional difficulties for the manipulation of THz waves. Recently, metasurfaces, with their unique capability of electromagnetic waves manipulation, have indisputably become the most suitable platform for manipulating THz waves. Taking the advantage of the strong localization capability derived from the sub-wavelength unit cell, metasurfaces have been demonstrated versatile devices that enable to manipulate THz waves efficiently, including THz modulators [10–15], absorbers [16–20] and bio-sensors [21–25].

PIT, a quantum interference phenomenon occurring in a three levels atomic system [26], is able to induce a narrow transparency region in the absorptive spectrum. And PIT is the result of interference between the bright mode which couples with free space strongly and dark mode which couples with free space weakly, which leads to the complicated experimental set-up in quantum optical implementations. The bright mode is directly activated by incident light, yet the dark mode can only be excited through the localized field formed by the coupling of the bright mode and the excitation light field [27,28]. For instance, a simple

* Corresponding authors at: School of Mathematical and Physical Sciences, Wuhan Textile University, Wuhan 430200, PR China.
E-mail addresses: zhuwei@wtu.edu.cn (W. Zhu), shxwang@wtu.edu.cn (S. Wang).

https://doi.org/10.1016/j.optlastec.2023.109431
Received 27 December 2022; Received in revised form 4 March 2023; Accepted 26 March 2023
Available online 12 April 2023
0030-3992/© 2023 Elsevier Ltd. All rights reserved.

metal bar can be regarded as an optical dipole. Therefore, it could function as bright mode in PIT system [29]. Therefore, it is convenient to construct the destructive interference between two excitation channels involving a bright mode and a dark mode in metasurfaces. Moreover, metasurfaces enable enhancing the light-matter interaction by localizing the electromagnetic waves in the sub-wavelength area. In this way, PIT-like metasurfaces have recently been extensively investigated due to the capability for flexible THz radiation manipulation based on the design of *meta*-atoms [30–40]. Nevertheless, just like other THz metasurfaces, PIT-like metasurfaces are also restricted by the conventional micro-processes, such as photolithography, reactive ion etching, etc., which are not only high-cost, time-consuming, but also impossible to fabricate in large-area.

Laser direct writing method has been adjusted to fabricate patterns and microstructures/nanostructures at present [41,42]. Recent years have witnessed a spurt of progress in graphene oxide, graphene and its applications in various electronic devices. Specifically, featuring excellent flexibility, transparency, conductivity, and mechanical robustness, graphene has emerged as a versatile material for flexible electronics. In particular, laser fabrication for graphene exhibits obvious superiority which can fabricate flexible electronics applications [43], such as supercapacitors [44], sensor [45], actuators [46].

In this work, we have proposed a novel method to fabricate ultra-fast, large-area, flexible THz metasurface by using a 515 nm pico-second laser, a scan lens, and a matching scanning system. It is noting that the graphene assembly film (GAF) composed of flexible PIT-like THz metasurface is obtained by reducing graphene oxide films, which possesses a series of advantages such as superb flexibility, lightweight and outstanding mechanical stability. Combining the scan lens and the fast-scanning system, a flexible THz PIT-like metasurface with a size of 229 mm × 305 mm and a resolution of 50 μm can be fabricated. Obviously, the limit resolution can be further improved by optimized the laser energy densities and the repetition rate. The PIT effect derives from the proposed flexible THz metasurface fabricated by LDW has been demonstrated by numerical simulations and experimental measurements, and the transparency window appears at 0.509 THz. To further validate the working mechanism of proposed PIT-like metasurface, the theoretical analysis based on the coupled harmonic oscillator model and distributions of the electric field and magnetic field have been investigated. Undoubtedly, the good group delay performance accompanying PIT effect is also calculated, which has potential applications in the field of slow light and THz communication. Therefore, large-area patterns can

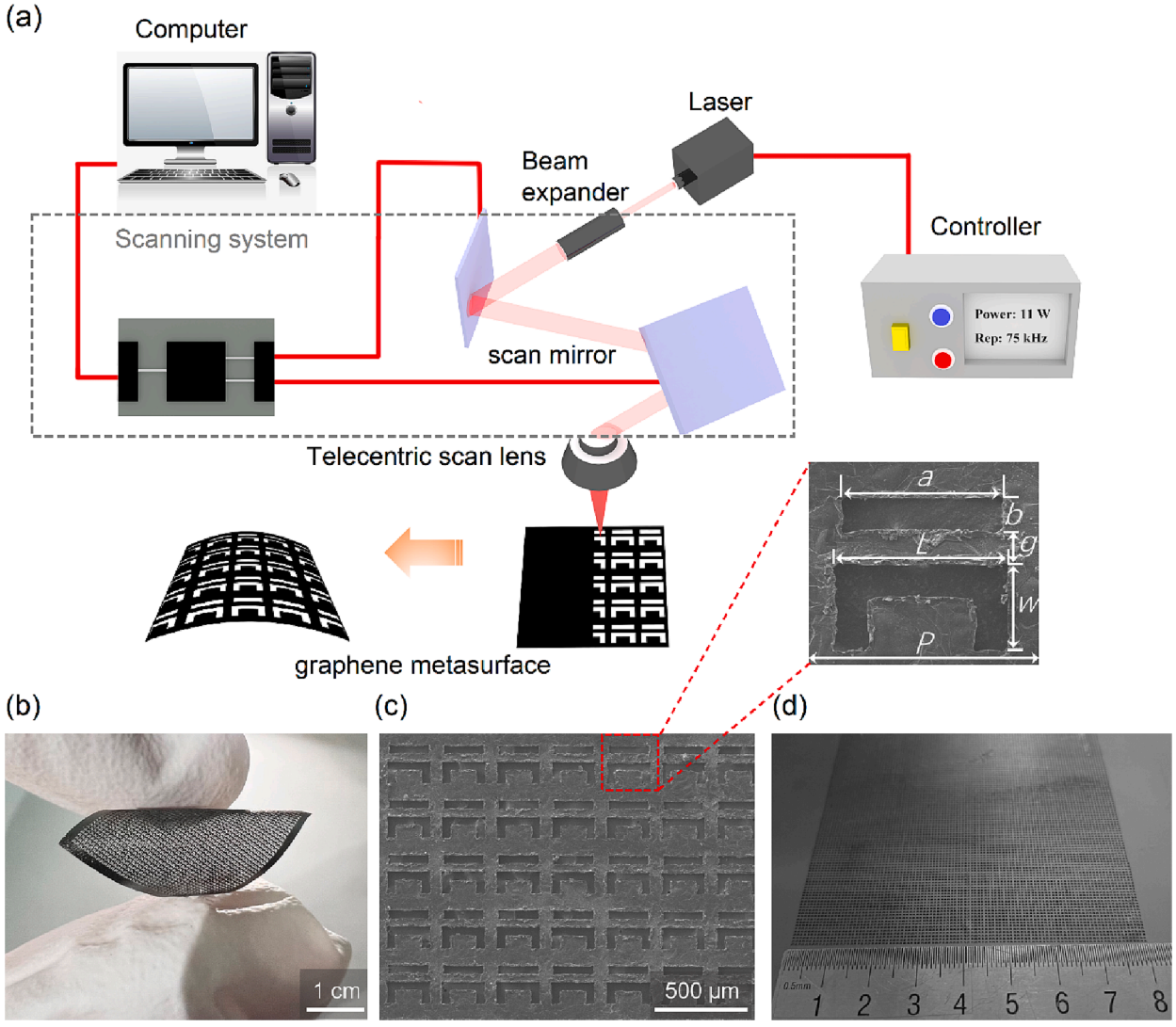

Fig. 1. Schematic diagram of the fabrication setup and the designed free-standing PIT-like metasurface. (a) Schematic illustration of the LDW system. (b) The sample of the flexible PIT-like metasurface (3 cm × 3 cm). (c) SEM image of the fabricated GAF sample and the geometric parameters have been listed in the enlarged diagram. (d) The sample of the fabricated metasurface (8 cm × 8 cm).

be easily fabricated in different substrates by using the proposed LDW method, which proves that the proposed new fabricated method is able to provide a new idea for THz devices.

2. Materials and design

The schematic of the LDW fabrication system is depicted in Fig. 1(a). It is composed of a picosecond solid-state laser (pulse width: 1.5 ps, adjustable repetition rate: 50–500 kHz) with an output wavelength of 515 nm, a beam expander, a telecentric scan lens, and a matching scanning system, which consists of two scanning mirrors that can tilt the laser beam toward *x*- and *y*-directions, respectively. Therefore, LDW system is able to fabricate the arbitrary patterns on various different substrates by laser ablation such as copper, graphene, etc. The GAF with a thickness of 14.5 μm is used to fabricate the THz PIT-like metasurface, which possesses flexible character to adapt to arbitrary external shape.

Compared with the traditional fabricated methods of THz devices, LDW fabrication system can omit the complicated steps in micro-nano processing technology such as spin-coating, exposure, development and lift-off. In addition, the fast-tilting speed of scanning mirrors can guarantee the fast speed of the fabrication and large-scale sample whose effective area can reach 229 mm × 305 mm. However, it is inevitable that the focus spot would undergo the distortion from circular spot to elliptical spot for large deflection angles, which will decrease the fabrication resolution. To eliminate the elliptical distortion of the focus spot, a telecentric scan lens is introduced in the system. Firstly, the GAF spread all over the translation stage horizontally. Then, the laser beam created the trace structure on the surface of the GAF with a precisely dosed energy input (repetitive frequency:100 kHz, power:3W), and repeated around 30–50 times depending on the actual fabrication depth. Finally, the proposed metasurface can be obtained by LDW method. The photo and the scanning electron microscope (SEM) image of the flexible PIT-like metasurface are shown in Fig. 1(b) and (c). It is obvious that the flexible THz devices can be fabricated by LDW system which can ablate the GAF with good mechanical properties. And the size of the unit cell fabricated by LDW system is consistent with our optimized geometric size: $L = 240$ μm, $W = 120$ μm, $a = 220$ μm, $b = 50$ μm and the distance between the two nanoslots is $g = 40$ μm. In addition, a larger sample of 8 cm × 8 cm was easily fabricated by LDW rapidly in order to better exhibit its potential for processing graphene, which is shown in Fig. 1(d). More importantly, any desired patterns can be prepared by the simple and rapid approach. The unique property makes LDW method a prospective replacement for a high-speed fabrication of large-scale and high-quality samples. In the simulation, the conductivity of GAF is set to 1.1×10^6 S m^{-1} which is extracted from the reflective spectrum of experimental data and the period of the unit cell P is set to 300 μm, which enable ensure the PIT window appears at 0.509 THz. It is a remarkable fact that the limit resolution of fabrication is determined by the thickness of GAF, the threshold will increase with the decrease of the thickness of GAF.

The preparation steps of the GAF are as follows (Fig. 2(a)). Firstly, the GO slurry was diluted with ultrapure water and then stirred evenly to obtain a GO suspension with a concentration of 15 mg mL^{-1}. The GO assembly film was obtained after the evaporation of GO suspension in a glass container at room temperature. Then, GO assembly film was annealed at high temperatures of 1300 °C for 2 h and 3000 °C for 1 h in a high-temperature furnace which was in Ar gas atmosphere. Thus, the pre-GAF was obtained. Finally, the GAF was sandwiched into two polyethylene terephthalate (PET) substrates and statically calendered for 0.5 h at room temperature with a pressure of 100 MPa, and the GAF with the dense structure were obtained. As shown in Fig. 2(b) and (c), the dense layer-stack structure of the GAF with a thickness of 14.5 μm can be found in the cross-sectional scanning electron microscope (SEM, JSM-7100F) image.

The GAF has a high electrical conductivity of 1.1×10^6 S m^{-1}, which was obtained by four probe test method. The GAF with such high electrical conductivity has a highly graphitized structure, which can be proved by the X-ray diffraction (XRD) patterns. The XRD patterns were performed by X-ray D/MAX-RB instruments with Cu Ka radiation. The sharp diffraction peak of (0 0 2) crystal plane laid at $2\theta = 26.5$ show an interlayer distance of 0.336 nm of the GAF (Fig. 2(d)). The (0 0 4) crystal plane and Raman spectroscopy of the GAF also illustrate the highly graphitized structure of the GAF. The Raman spectroscopy of the GAF was collected by a Renishaw Raman Spectrometer. The weak D band located in 1344 cm^{-1} and the obvious G band located in 1579 cm^{-1} (inset of Fig. 2(d)) show a low-defect and highly graphitized structure of the GAF.

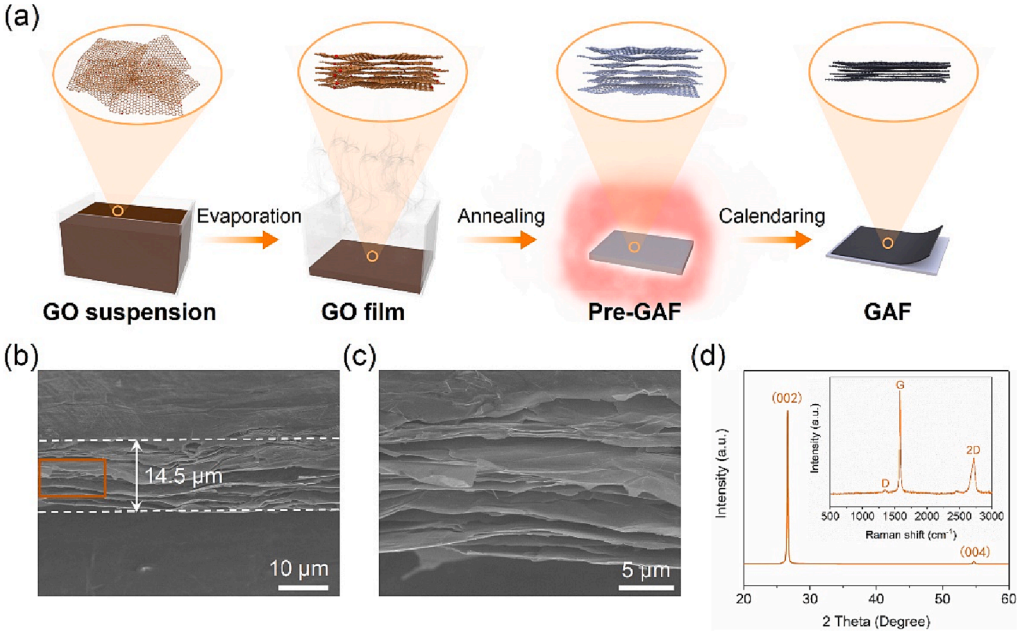

Fig. 2. Characterization of GAF. (a) Schematic illustration of GAF preparation process. SEM images of GAF (b) cross-section and (c) the locally magnified. (d) XRD pattern of GAF (Inset: Raman spectrum of GAF).

3. Results and discussion

Babinet's principle [47–50] associates not only transmittance and reflectance between a structure and its complement, but also the field modal profiles of the electromagnetic resonances as well as effective material parameters — a critical concept for metamaterials. The PIT of complementary asymmetric structure appears as a sharp peak in the reflectance spectrum, in contrast to PIT in positive structure, which appears as a transparent window in the transmittance spectra. In order to investigate the mechanism of the PIT characteristic, we perform numerical simulated reflectance spectra based on the Babinet's principle, which links the field modal profiles of electromagnetic resonances and effective material properties, in addition to transmittance and reflectance between a structure and its complement [51]. Simulated reflectance spectra with the results of two separate nanoslots illustrates the formation process, as shown in Fig. 3(a). The single split-ring resonator (SRR) slot array exhibits a strong resonance at 0.44 THz when the excitation field is parallel to the *y*-axis. And the reflectance spectra of the closed wire resonator (CWR) slot array excited at 0.64 THz is similar to SRR slot. We define the closed wire resonator (CWR) as bright mode while the SRR as quasi-dark mode (ref. [27,52,53] regards it as a bright mode). When the two slots are integrated within one unit, we can observe a sharp transparency peak of 91% at 0.509 THz between the resonant frequency located at 0.43 THz and 0.68 THz. The bright mode couples with the quasi-dark mode, thereby forming an analogue of the PIT effect.

To explore the formation mechanism of the PIT effect, we use a simple two-particle PIT model [54]. By introducing this theory, where we consider a bright (designated as "particle A") and a quasi-dark (designated as "particle B") particle coupled to the incident THz electric field$\boldsymbol{E} = E_0 e^{i\omega t}$, the effectiveness of this PIT can be analyzed. Hence, the analytical model can be described by the following coupled differential equations [27,39,54]:

$$\ddot{x}_a(t) + \gamma_a \dot{x}_a(t) + \omega_a^2 x_a(t) + \kappa^2 x_b(t) = \frac{q_a E}{m_a} \tag{1}$$

$$\ddot{x}_b(t) + \gamma_b \dot{x}_b(t) + \omega_b^2 x_b(t) + \kappa^2 x_a(t) = \frac{q_b E}{m_b} \tag{2}$$

where (x_a, x_b), (q_a, q_b), (m_a, m_b), (ω_a, ω_b) and (γ_a, γ_b) represent

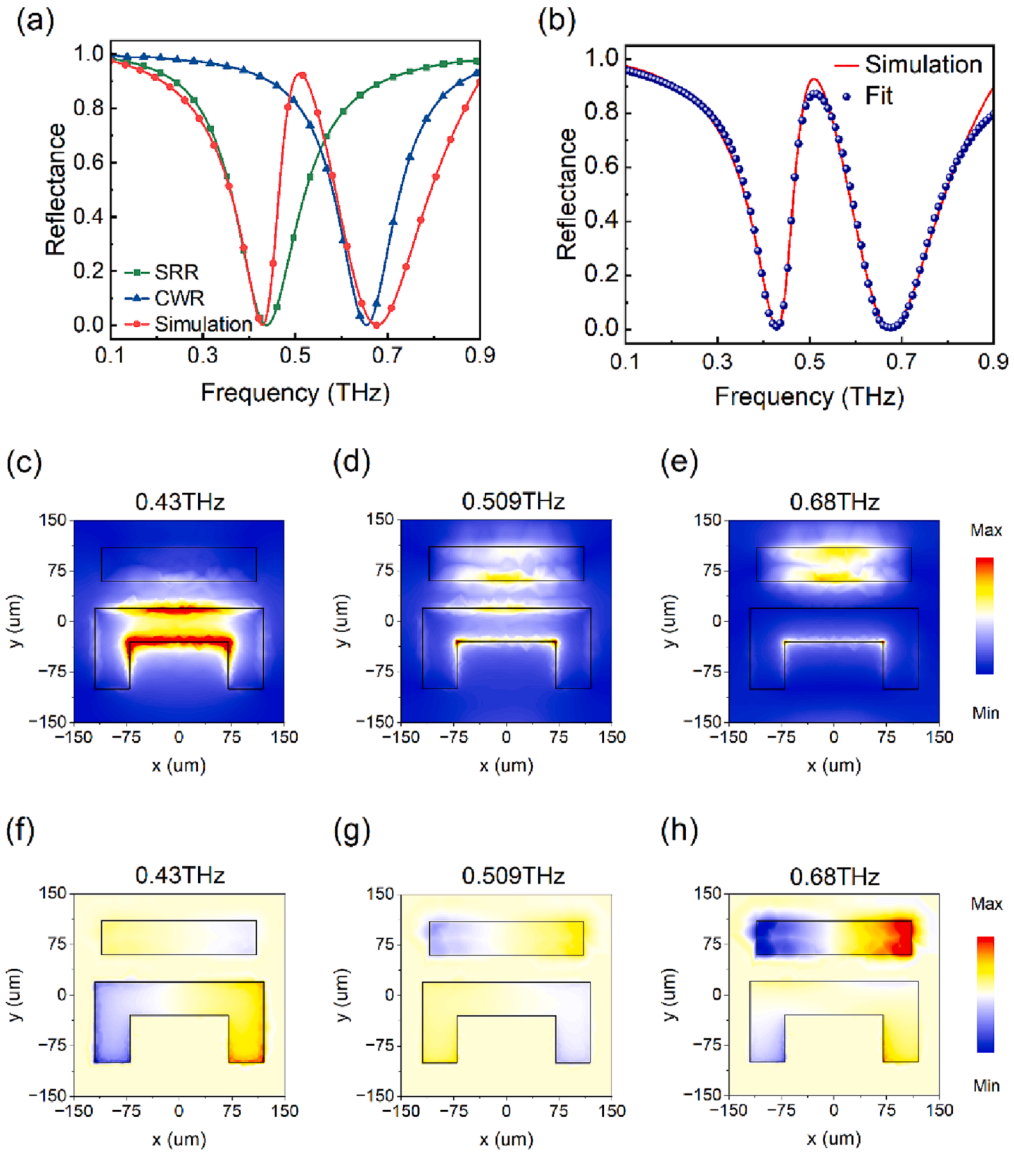

Fig. 3. (a) The simulated reflectance spectra of the integrated PIT structure as well as the couple units (SRR and CWR). (b) Simulated data and the theoretically fitting calculations by the two particles model. (c)–(e) simulation of $|\boldsymbol{E}|$ distributions at the resonant frequency of (c) $f = 0.43$ THz, (d) $f = 0.509$ THz, (e) $f = 0.68$ THz. (f)–(h) The simulation of $\boldsymbol{H_z}$ distributions at the reflectance dips and peak.

displacements, the effective charge, effective masses of two particles (the SRR and CWR elements), resonance angular frequencies, and the loss factor of the particle A (B), respectively. In the theoretical model, the resonance frequencies of the bright and the quasi-dark modes are kept constant which are calculated to be around 4.2×10^{12} rad·s^{-1} and 2.7×10^{12} rad·s^{-1}. The values of the loss factors are obtained from the linewidths of the curves which are calculated to be about 8.2×10^{11} rad·s^{-1} and 4.1×10^{11} rad·s^{-1}, respectively. And κ defines the coupling coefficient between the bright and quasi-dark particles. In the above coupled equations, we substitute $q_b = \frac{q_a}{A}$ and $m_b = \frac{m_a}{B}$, where A and B are the dimensionless constants, which represent the free space coupling strengths of bright and the quasi-dark modes with the incident THz light, respectively. Some special PIT-like metasurfaces, involving the proposed asymmetric planar metasurface, the split-closed rings metasurface [52] and the cut-continuous strips metasurface [55], incorporate a "quasi-dark" element, which is also activated by the incident wave via near-field coupling in a certain extent. Therefore, q_b cannot be neglected anymore because of the quantity q_b proportional to the coupling strength between the quasi-dark element and the incident wave under the circumstances [56].

By solving the above coupled equations Eq. (1) and Eq. (2), x_a and x_b can be obtained by the following equations:

$$x_a = \frac{\left(\left(\frac{B}{A}\right)\kappa^2 + \left(\omega^2 - \omega_b^2 + i\omega\gamma_b\right)\right)\left(\frac{q_a E}{m_a}\right)}{\kappa^4 - (\omega^2 - \omega_a^2 + i\omega\gamma_a)(\omega^2 - \omega_b^2 + i\omega\gamma_b)} \tag{3}$$

$$x_b = \frac{\left(\left(\frac{B}{A}\right)\kappa^2 + \left(\omega^2 - \omega_a^2 + i\omega\gamma_a\right)\right)\left(\frac{q_a E}{m_a}\right)}{\kappa^4 - (\omega^2 - \omega_a^2 + i\omega\gamma_a)(\omega^2 - \omega_b^2 + i\omega\gamma_b)} \tag{4}$$

The effective polarization of the graphene metamaterial is expressed by:

$$P = q_a x_a + q_b x_b \tag{5}$$

Consequently, the linear susceptibility χ of the graphene metamaterial can be written as:

$$\chi = \frac{P}{\varepsilon_0 E} = \frac{K}{A^2 B}\left(\begin{array}{c} \frac{A(B+1)\kappa^2 + A^2(\omega^2 - \omega_b^2) + B(\omega^2 - \omega_a^2)}{\kappa^4 - \left(\omega^2 - \omega_a^2 - i\omega\gamma_a\right)\left(\omega^2 - \omega_b^2 - i\omega\gamma_b\right)} \\ +i\omega\frac{A^2\gamma_b + B\gamma_a}{\kappa^4 - \left(\omega^2 - \omega_a^2 - i\omega\gamma_a\right)\left(\omega^2 - \omega_b^2 - i\omega\gamma_b\right)} \end{array}\right) \tag{6}$$

The simulated reflectance in Fig. 3(b) is fitted by the imaginary part of the nonlinear susceptibility expression. Here, $Re[\chi]$ stands for the dispersion and $Im[\chi]$ shows the absorption (loss) within the medium. The Kramer-Kronig relations state that the transmission coefficient is defined as $T = 1 - Im[\chi]$ which comes from the conservation of energy relation $T + A = 1$ (normalized to unity), where $A = Im[\chi]$ is the absorption/losses in the medium [39]. The designed metasurface we proposed has a complementary relationship with the analytical coupled equations due to Babinet's principle the proof of the behavior of interchange between the reflectance and the transmittance when the polarization direction of the light is rotated by 90°. In our case, we can calculate the reflection utilizing the transmission equation in normal fabricated structure. Moreover, we disregard further non-resonant scattering losses since they have no impact on the system's performance. By substituting the fitting parameters $\gamma_a, \gamma_b, \omega_a, \omega_b$ and by putting $A = 6.5$ and $B = 3.2$, we plot the theoretically fitting reflectance spectra in Fig. 3(b), which exhibit good agreement with the corresponding numerically simulated curves.

To further understand the mechanism physics, the numerical simulations electric field $\boldsymbol{E} = \sqrt{E_x^2 + E_y^2 + E_z^2}$ and z component of the magnetic field distributions are presented in Fig. 3(c)-(h). Please notice that, for complementary structure, Babinet's principle states that each electric field component and its magnetic counterpart should be interchangeable if the incident polarizations are perpendicular. It is quite distinct that the two slots are excited individually acting as the bright mode in which the $\boldsymbol{E}$-field distributions are confined at the inner top and bottom of each slot at the reflectance dips $f = 0.43$ THz and 0.68 THz, as shown in Fig. 3(c)-(e). The PIT phenomenon is attributed to the simultaneous excitation of the two slots at $f = 0.509$ THz, which verifies that the transparency window is mainly related with the weak hybridization of two dipolar modes.

In Fig. 3(f)-(h), the $\boldsymbol{H}_z$ (z component of the magnetic field) distributions are clearly expressed in the *xoy* plane. Only SRR or CWR is strongly excited at the resonant frequencies but both are excited in 0.509 THz. At relatively low resonance (CWR is excited by the incident wave) the field is out-of-phase while at relatively high frequency they are in-phase, similar to two straight slots placed in parallel [57]. Moreover, we clearly observe the magnetic fields with comparable densities in the two resonators are out-of-phase. The PIT feature can be clearly obtained by the field components with quadrupolar symmetry. In other words, the phase destructive interference between the two anti-phase distribution modes leads to the transparency window so that the incident light propagating on the *meta*-atoms will be totally reflected as if no slots existed in the metal.

The measured reflectance spectrum is performed using terahertz time domain spectroscopy (THz-TDS), which is depicted in Fig. 4(a). The normal transmission spectrum from the sample is determined as $\left|\widetilde{T}(\omega)\right| = \left|\widetilde{E}_S(\omega)/\widetilde{E}_R(\omega)\right|$ where $\widetilde{E}_S(\omega)$ and $\widetilde{E}_R(\omega)$ are the electric field amplitude of the sample and reference, respectively [31]. We can experimentally observe a sharp reflectance peak in the asymmetry paired slots because of the weak hybridization of two resonant modes. The slight reduction of the reflectance peak intensity may be associated to the inaccuracies of graphene structure, likewise, broadening of the dips and peak widths. A remarkable feature of the PIT phenomenon is accompanied with strong dispersion, which causes a slow wave effect because of an alteration of the group velocity which is the inverse of the derivative of the wave number with respect to the angular frequency through the device. It is highly desired that the slow light of PIT effect in metasurface can be applied in strong interactions between light and matter and improved nonlinear effects. The group delay is a key metric to describe the slow wave performance in PIT system. The group delay is expressed as $t_g = -\frac{d\varphi}{d\omega}$ where φ and $\omega = 2\pi f$ refer to the reflection phase shift and angular frequency, respectively [58]. Fig. 4(b) shows the calculated reflection phase shift and group delay of our designed metasurface. The arctangent-based definition of the phase analysis is wrapped in the region$[-\pi, +\pi]$. However, true phase values may exceed the 2π range, which cause discontinuities in the recovered phase. We identify discontinuities on the wrapped phase and solve them to obtain the unwrapped phase. While a region of the positive group delay is realized near the transparency window, a strong slope of the phase shift can be seen. Around the resonance frequencies of dips, the metasurface is described as negative group delay. The positive and steepest phase slope is around the PIT window, and the sharp dispersion region which is depict in light yellow region leads to the maximum group delay of 9.93 ps. The result, such a large positive group delay, provides a strong evidence in the slow light capability of PIT metasurface. That is, the THz radiation experiences a delay of around 9.93 ps at 0.509 THz, where 91% of PIT reflectance is attained. This delay is comparable to the time delay of a 2979 μm distance of free space propagation. Our work will be strategically important in the practical applications of slow light applications devices.

4. Conclusions

In this work, a novel LDW system which can support high-speed, large-scale, and high-resolution fabrication of sample is applied to directly print THz PIT-like metesurface. The LDW system composed of picosecond laser with a focal spot 10 μm, telecentric scan lens, and the large 2D fabrication platform is able to fabricate the THz devices with an

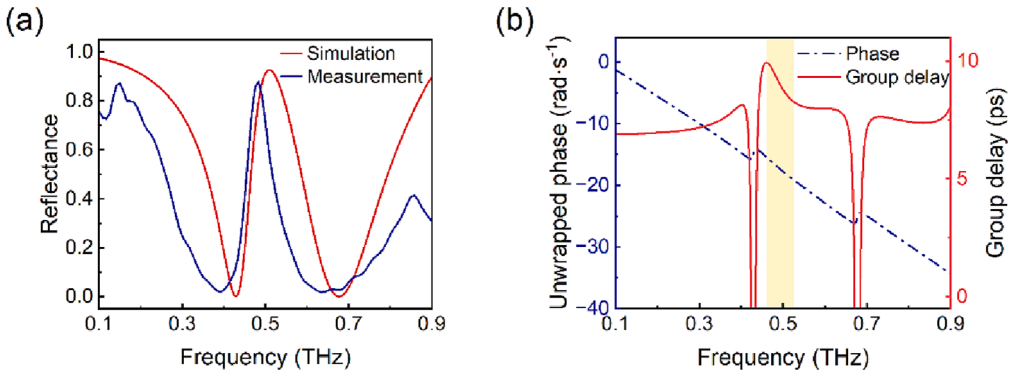

Fig. 4. (a) The simulated (red line) and measured reflectance curve (blue line). (b) The unwrapped phase (blue dash dot) and simulated group delay (red line) of the reflectance.

area of 229 mm × 305 mm. The speed of fabrication is mainly effected by the geometric configuration and complexity of the unit cell, while the scanning mirrors with the fast-tilting speed has been introduced in the LDW system. In addition, the large power of the picosecond laser (~8 W) and tunable repetition rate (50 ~ 500 kHz) can adjust the energy of ablation flexibly to adapt to different materials. In this way, using the GAF with ultra-high conductivity, we have designed and fabricated a THz PIT-like metasurface through both simulation and experimental studies. Accordingly, we employ the coupled harmonic oscillator model to describe the near field coupling between the nano-slots in metasurface that agrees well with the simulation results, and the inner physical mechanism has also been investigated by the distribution of electromagnetic field. The proposed novel ultra-fast and large-area, fabrication method dependent on LDW system can not only develop the THz PIT-like metasurface which shows strong potential in slow light applications but also open up a new way for the next generation THz devices.

CRediT authorship contribution statement

Bohan Zhang: Conceptualization, Investigation, Writing – original draft. **Xiaotian Huang:** Software, Writing – review & editing. **Ge Chen:** Visualization. **Zhe Wang:** Investigation. **Wei Qian:** Formal analysis. **Zixin Zhang:** Methodology. **Weiqi Cai:** Investigation. **Kang Du:** Data curation. **Cai Zhou:** Validation. **Tingting Wang:** Software. **Wei Zhu:** Project administration, Funding acquisition. **Daping He:** Supervision, Funding acquisition. **Shengxiang Wang:** Supervision, Writing – review & editing.

Declaration of Competing Interest

The authors declare that they have no known competing financial interests or personal relationships that could have appeared to influence the work reported in this paper.

Data availability

Data will be made available on request.

Acknowledgements

This work was financially supported by Foundation of Wuhan Textile University (20220609) and National Natural Science Foundation of China (Grant Nos. 51901163, 51701146 and 22279097).

References

[1] B. Ferguson, X.-C. Zhang, Materials for terahertz science and technology, Nat. Mater. 1 (2002) 26–33, https://doi.org/10.1038/nmat708.
[2] A. Kumar, M. Gupta, P. Pitchappa, N. Wang, P. Szriftgiser, G. Ducournau, R. Singh, Phototunable chip-scale topological photonics: 160 Gbps waveguide and demultiplexer for THz 6G communication, Nat. Commun. 13 (2022) 5404, https://doi.org/10.1038/s41467-022-32909-6.
[3] C. Wang, R. Zhou, Y. Huang, L. Xie, Y. Ying, Terahertz spectroscopic imaging with discriminant analysis for detecting foreign materials among sausages, Food Control. 97 (2019) 100–104, https://doi.org/10.1016/j.foodcont.2018.10.024.
[4] I. Jones, T.J. Rainsford, S.P. Mickan, D. Abbott, Ab initio molecular orbital theory: a tool for THz spectroscopic investigation, in: D. Abbott, Y.S. Kivshar, H.H. Rubinsztein-Dunlop, S. Fan (Eds.), Photonics Des. Technol. Packag. II, SPIE, Brisbane, Australia, 2005: p. 60381I. https://doi.org/10.1117/12.638131.
[5] X. Yang, X. Zhao, K. Yang, Y. Liu, Y. Liu, W. Fu, Y. Luo, Biomedical Applications of Terahertz Spectroscopy and Imaging, Trends Biotechnol. 34 (2016) 810–824, https://doi.org/10.1016/j.tibtech.2016.04.008.
[6] P.H. Siegel, Terahertz Technology in Biology and Medicine, IEEE Trans. Microw. Theory Tech. 52 (2004) 2438–2447, https://doi.org/10.1109/TMTT.2004.835916.
[7] E. Pickwell, V.P. Wallace, Biomedical applications of terahertz technology, J. Phys. Appl. Phys. 39 (2006) R301–R310, https://doi.org/10.1088/0022-3727/39/17/R01.
[8] P.H. Siegel, Terahertz technology, IEEE Trans. Microw. Theory Tech. 50 (2002) 910–928, https://doi.org/10.1109/22.989974.
[9] M. Tonouchi, Cutting-edge terahertz technology, Nat. Photonics. 1 (2007) 97–105, https://doi.org/10.1038/nphoton.2007.3.
[10] H.-T. Chen, W.J. Padilla, J.M.O. Zide, A.C. Gossard, A.J. Taylor, R.D. Averitt, Active terahertz metamaterial devices, Nature. 444 (2006) 597–600, https://doi.org/10.1038/nature05343.
[11] W.J. Padilla, A.J. Taylor, C. Highstrete, M. Lee, R.D. Averitt, Dynamical Electric and Magnetic Metamaterial Response at Terahertz Frequencies, Phys. Rev. Lett. 96 (2006), 107401, https://doi.org/10.1103/PhysRevLett.96.107401.
[12] L. Cong, N. Xu, J. Han, W. Zhang, R. Singh, A Tunable Dispersion-Free Terahertz Metadevice with Pancharatnam-Berry-Phase-Enabled Modulation and Polarization Control, Adv. Mater. 27 (2015) 6630–6636, https://doi.org/10.1002/adma.201502716.
[13] N.K. Grady, J.E. Heyes, D.R. Chowdhury, Y. Zeng, M.T. Reiten, A.K. Azad, A. J. Taylor, D.A.R. Dalvit, H.-T. Chen, Terahertz Metamaterials for Linear Polarization Conversion and Anomalous Refraction, Science. 340 (2013) 1304–1307, https://doi.org/10.1126/science.1235399.
[14] N.-H. Shen, M. Massaouti, M. Gokkavas, J.-M. Manceau, E. Ozbay, M. Kafesaki, T. Koschny, S. Tzortzakis, C.M. Soukoulis, Optically Implemented Broadband Blueshift Switch in the Terahertz Regime, Phys. Rev. Lett. 106 (2011), 037403, https://doi.org/10.1103/PhysRevLett.106.037403.
[15] Y.K. Srivastava, M. Manjappa, L. Cong, H.N.S. Krishnamoorthy, V. Savinov, P. Pitchappa, R. Singh, A Superconducting Dual-Channel Photonic Switch, Adv. Mater. 30 (2018) 1801257, https://doi.org/10.1002/adma.201801257.
[16] H. Tao, C.M. Bingham, A.C. Strikwerda, D. Pilon, D. Shrekenhamer, N.I. Landy, K. Fan, X. Zhang, W.J. Padilla, R.D. Averitt, Highly flexible wide angle of incidence terahertz metamaterial absorber: Design, fabrication, and characterization, Phys. Rev. B. 78 (2008), 241103, https://doi.org/10.1103/PhysRevB.78.241103.
[17] Y.Z. Cheng, W. Withayachumnankul, A. Upadhyay, D. Headland, Y. Nie, R.Z. Gong, M. Bhaskaran, S. Sriram, D. Abbott, Ultrabroadband Plasmonic Absorber for Terahertz Waves, Adv. Opt. Mater. 3 (2015) 376–380, https://doi.org/10.1002/adom.201400368.
[18] P.C. Wu, N. Papasimakis, D.P. Tsai, Self-Affine Graphene Metasurfaces for Tunable Broadband Absorption, Phys. Rev. Appl. 6 (2016), 044019, https://doi.org/10.1103/PhysRevApplied.6.044019.
[19] C. Chen, S. Can, J. Schalch, X. Zhao, G. Duan, R.D. Averitt, X. Zhang, Ultrathin Terahertz Triple-Band Metamaterial Absorbers: Consideration of Interlayer Coupling, Phys. Rev. Appl. 14 (2020), 054021, https://doi.org/10.1103/PhysRevApplied.14.054021.
[20] X. Cheng, R. Huang, J. Xu, X. Xu, Broadband Terahertz Near-Perfect Absorbers, ACS Appl. Mater. Interfaces. 12 (2020) 33352–33360, https://doi.org/10.1021/acsami.0c06162.
[21] S.H. Huang, J. Li, Z. Fan, R. Delgado, G. Shvets, Monitoring the effects of chemical stimuli on live cells with metasurface-enhanced infrared reflection spectroscopy, Lab. Chip. 21 (2021) 3991–4004, https://doi.org/10.1039/D1LC00580D.

[22] A. Ahmadivand, B. Gerislioglu, Z. Ramezani, A. Kaushik, P. Manickam, S. A. Ghoreishi, Functionalized terahertz plasmonic metasensors: Femtomolar-level detection of SARS-CoV-2 spike proteins, Biosens. Bioelectron. 177 (2021), 112971, https://doi.org/10.1016/j.bios.2021.112971.
[23] Z. Zhang, C. Zhong, F. Fan, G. Liu, S. Chang, Terahertz polarization and chirality sensing for amino acid solution based on chiral metasurface sensor, Sens. Actuators B Chem. 330 (2021), 129315, https://doi.org/10.1016/j.snb.2020.129315.
[24] Z. Bai, Y. Liu, R. Kong, T. Nie, Y. Sun, H. Li, T. Sun, C. Pandey, Y. Wang, H. Zhang, Q. Song, G. Liu, M. Kraft, W. Zhao, X. Wu, L. Wen, Near-field Terahertz Sensing of HeLa Cells and Pseudomonas Based on Monolithic Integrated Metamaterials with a Spintronic Terahertz Emitter, ACS Appl. Mater. Interfaces. 12 (2020) 35895–35902, https://doi.org/10.1021/acsami.0c08543.
[25] A. Ahmadivand, B. Gerislioglu, P. Manickam, A. Kaushik, S. Bhansali, M. Nair, N. Pala, Rapid Detection of Infectious Envelope Proteins by Magnetoplasmonic Toroidal Metasensors, ACS Sens. 2 (2017) 1359–1368, https://doi.org/10.1021/acssensors.7b00478.
[26] S.E. Harris, J.E. Field, A. Imamoğlu, Nonlinear optical processes using electromagnetically induced transparency, Phys. Rev. Lett. 64 (1990) 1107–1110, https://doi.org/10.1103/PhysRevLett.64.1107.
[27] M. Chen, Z. Xiao, F. Lv, Z. Cui, Q. Xu, Dynamically Tunable Electromagnetically Induced Transparency-Like Effect in Terahertz Metamaterial Based on Graphene Cross Structures, IEEE J. Sel. Top. Quantum Electron. 28 (2022) 1–9, https://doi.org/10.1109/JSTQE.2021.3091147.
[28] Z. Jia, L. Huang, J. Su, B. Tang, Tunable Electromagnetically Induced Transparency-Like in Graphene metasurfaces and its Application as a Refractive Index Sensor, J. Light. Technol. 39 (2021) 1544–1549, https://doi.org/10.1109/JLT.2020.3035041.
[29] S. Zhang, D.A. Genov, Y. Wang, M. Liu, X. Zhang, Plasmon-Induced Transparency in Metamaterials, Phys. Rev. Lett. 101 (2008), 047401, https://doi.org/10.1103/PhysRevLett.101.047401.
[30] R. Singh, C. Rockstuhl, F. Lederer, W. Zhang, Coupling between a dark and a bright eigenmode in a terahertz metamaterial, Phys. Rev. B. 79 (2009), 085111, https://doi.org/10.1103/PhysRevB.79.085111.
[31] J. Gu, R. Singh, X. Liu, X. Zhang, Y. Ma, S. Zhang, S.A. Maier, Z. Tian, A.K. Azad, H.-T. Chen, A.J. Taylor, J. Han, W. Zhang, Active control of electromagnetically induced transparency analogue in terahertz metamaterials, Nat. Commun. 3 (2012) 1151, https://doi.org/10.1038/ncomms2153.
[32] Z. Bai, G. Huang, Plasmon dromions in a metamaterial via plasmon-induced transparency, Phys. Rev. A. 93 (2016), https://doi.org/10.1103/PhysRevA.93.013818.
[33] Z. Li, Y. Ma, R. Huang, R. Singh, J. Gu, Z. Tian, J. Han, W. Zhang, Manipulating the plasmon-induced transparency in terahertz metamaterials, Opt. Express. 19 (2011) 8912–8919, https://doi.org/10.1364/OE.19.008912.
[34] H. Cheng, S. Chen, P. Yu, X. Duan, B. Xie, J. Tian, Dynamically tunable plasmonically induced transparency in periodically patterned graphene nanostrips, Appl. Phys. Lett. 103 (2013), 203112, https://doi.org/10.1063/1.4831776.
[35] R. Singh, I.A.I. Al-Naib, Y. Yang, D. Roy Chowdhury, W. Cao, C. Rockstuhl, T. Ozaki, R. Morandotti, W. Zhang, Observing metamaterial induced transparency in individual Fano resonators with broken symmetry, Appl. Phys. Lett. 99 (2011), 201107, https://doi.org/10.1063/1.3659494.
[36] M. Manjappa, Y.K. Srivastava, R. Singh, Lattice-induced transparency in planar metamaterials, Phys. Rev. B. 94 (2016), 161103, https://doi.org/10.1103/PhysRevB.94.161103.
[37] S.-Y. Chiam, A.A. Bettiol, R. Singh, W. Zhang, C. Rockstuhl, F. Lederer, Analogue of Electromagnetically Induced Transparency in a Terahertz Metamaterial, Phys. Rev. B. 80 (2009), 153103, https://doi.org/10.1103/PhysRevB.80.153103.
[38] N. Papasimakis, V.A. Fedotov, N.I. Zheludev, S.L. Prosvirnin, Metamaterial Analog of Electromagnetically Induced Transparency, Phys. Rev. Lett. 101 (2008), 253903, https://doi.org/10.1103/PhysRevLett.101.253903.
[39] R. Yahiaoui, J.A. Burrow, S.M. Mekonen, A. Sarangan, J. Mathews, I. Agha, T. A. Searles, Electromagnetically induced transparency control in terahertz metasurfaces based on bright-bright mode coupling, Phys. Rev. B. 97 (2018), 155403, https://doi.org/10.1103/PhysRevB.97.155403.
[40] L. Cong, R. Singh, Symmetry-Protected Dual Bound States in the Continuum in Metamaterials, Adv. Opt. Mater. 7 (2019) 1900383, https://doi.org/10.1002/adom.201900383.
[41] Y.-Q. Liu, J.-W. Mao, Z.-D. Chen, D.-D. Han, Z.-Z. Jiao, J.-N. Ma, H.-B. Jiang, H. yang, Three-dimensional micropatterning of graphene by femtosecond laser direct writing technology, Opt. Lett. 45 (2020) 113, https://doi.org/10.1364/OL.45.000113.
[42] Z.-Z. Jiao, H. Zhou, X.-C. Han, D.-D. Han, Y.-L. Zhang, Photothermal responsive slippery surfaces based on laser-structured graphene@PVDF composites, J. Colloid Interface Sci. 629 (2023) 582–592, https://doi.org/10.1016/j.jcis.2022.08.153.
[43] R. You, Y. Liu, Y. Hao, D. Han, Y. Zhang, Z. You, Laser Fabrication of Graphene-Based Flexible Electronics, Adv. Mater. 32 (2020) 1901981, https://doi.org/10.1002/adma.201901981.
[44] X.-Y. Fu, Q. Cai, J.-N. Ma, L. Zhu, D.-D. Han, Y.-L. Zhang, Free-standing and flexible graphene supercapacitors of high areal capacitance fabricated by laser holography reduction of graphene oxide, Appl. Phys. Lett. 118 (2021), 071601, https://doi.org/10.1063/5.0038508.
[45] Y. Qiao, Y. Wang, H. Tian, M. Li, J. Jian, Y. Wei, Y. Tian, D.-Y. Wang, Y. Pang, X. Geng, X. Wang, Y. Zhao, H. Wang, N. Deng, M. Jian, Y. Zhang, R. Liang, Y. Yang, T.-L. Ren, Multilayer Graphene Epidermal Electronic Skin, ACS Nano. 12 (2018) 8839–8846, https://doi.org/10.1021/acsnano.8b02162.
[46] H. Cheng, F. Zhao, J. Xue, G. Shi, L. Jiang, L. Qu, One Single Graphene Oxide Film for Responsive Actuation, ACS Nano. 10 (2016) 9529–9535, https://doi.org/10.1021/acsnano.6b04769.
[47] F. Falcone, T. Lopetegi, M.A.G. Laso, J.D. Baena, J. Bonache, M. Beruete, R. Marqués, F. Martín, M. Sorolla, Babinet Principle Applied to the Design of Metasurfaces and Metamaterials, Phys. Rev. Lett. 93 (2004), 197401, https://doi.org/10.1103/PhysRevLett.93.197401.
[48] A. Bitzer, A. Ortner, H. Merbold, T. Feurer, M. Walther, Terahertz near-field microscopy of complementary planar metamaterials: Babinet's principle, Opt. Express. 19 (2011) 2537, https://doi.org/10.1364/OE.19.002537.
[49] Y.L. Loo, H.G. Wang, H. Zhang, C.K. Ong, Miniaturized power limiter metasurface based on Fano-type resonance and Babinet principle, Opt. Express. 24 (2016) 20816, https://doi.org/10.1364/OE.24.020816.
[50] M. Hrtoň, A. Konečná, M. Horák, T. Šikola, V. Křápek, Plasmonic Antennas with Electric, Magnetic, and Electromagnetic Hot Spots Based on Babinet's Principle, Phys. Rev. Appl. 13 (2020), 054045, https://doi.org/10.1103/PhysRevApplied.13.054045.
[51] T. Zentgraf, T.P. Meyrath, A. Seidel, S. Kaiser, H. Giessen, C. Rockstuhl, F. Lederer, Babinet's principle for optical frequency metamaterials and nanoantennas, Phys. Rev. B. 76 (2007), 033407, https://doi.org/10.1103/PhysRevB.76.033407.
[52] C. Liu, Y. Xu, H. Liu, M. Lin, S. Zha, Switchable Metamaterial With Terahertz Buffering and Absorbing Performance, IEEE Photonics J. 13 (2021) 1–8, https://doi.org/10.1109/JPHOT.2021.3107533.
[53] K. Liu, Y. Li, K. Qin, T. Cao, Tuning of Classical Electromagnetically Induced Reflectance in Babinet Chalcogenide Metamaterials, IScience. 23 (2020), 101367, https://doi.org/10.1016/j.isci.2020.101367.
[54] R. Yahiaoui, M. Manjappa, Y.K. Srivastava, R. Singh, Active control and switching of broadband electromagnetically induced transparency in symmetric metadevices, Appl. Phys. Lett. 111 (2017), 021101, https://doi.org/10.1063/1.4993428.
[55] C.-Y. Chen, I.-W. Un, N.-H. Tai, T.-J. Yen, Asymmetric coupling between subradiant and superradiant plasmonic resonances and its enhanced sensing performance, Opt. Express. 17 (2009) 15372–15380, https://doi.org/10.1364/OE.17.015372.
[56] F.-Y. Meng, Q. Wu, D. Erni, K. Wu, J.-C. Lee, Polarization-Independent Metamaterial Analog of Electromagnetically Induced Transparency for a Refractive-Index-Based Sensor, IEEE Trans. Microw. Theory Tech. 60 (2012) 3013–3022, https://doi.org/10.1109/TMTT.2012.2209455.
[57] T. Wang, Y. Zhang, Z. Hong, Z. Han, Analogue of electromagnetically induced transparency in integrated plasmonics with radiative and subradiant resonators, Opt. Express. 22 (2014) 21529–21534, https://doi.org/10.1364/OE.22.021529.
[58] X. He, X. Yang, G. Lu, W. Yang, F. Wu, Z. Yu, J. Jiang, Implementation of selective controlling electromagnetically induced transparency in terahertz graphene metamaterial, Carbon. 123 (2017) 668–675, https://doi.org/10.1016/j.carbon.2017.08.016.